Materials Chemistry and Physics 296 (2023) 127181

Contents lists available at ScienceDirect

Materials Chemistry and Physics

journal homepage: www.elsevier.com/locate/matchemphys

Improving the soft magnetic properties of binder jet printed iron-silicon alloy through boron addition

Geeta Kumari [a,d,*], Thang Q. Pham [b], Hawke Suen [c], Tanzilur Rahman [a], Patrick Kwon [c], Shanelle N. Foster [b], Carl J. Boehlert [a]

[a] Department of Chemical Engineering & Materials Science, Michigan State University, USA
[b] Department of Electrical & Computer Engineering, Michigan State University, USA
[c] Department of Mechanical Engineering, Michigan State University, USA
[d] Department of Metallurgical & Materials Engineering, Indian Institute of Technology, Madras, India

HIGHLIGHTS

- Magnetic property and microstructural characterization of Fe–Si alloys, processed using binder jet printing, were performed.
- The effect of 0.25 wt% B addition as a sintering additive was studied and compared with the samples without B.
- Fe–5%Si-0.25%B sample sintered at 1200 °C exhibited the best combination of magnetic properties among all the printed samples.
- Compared to elemental powder, an improvement in permeability and coercivity was exhibited by the pre-alloyed powder mixture.

GRAPHICAL ABSTRACT

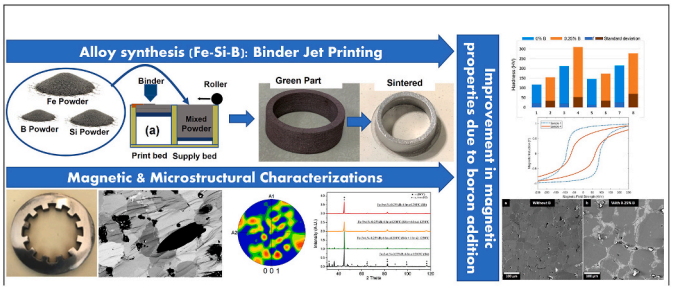

ARTICLE INFO

Keywords:
Additive manufacturing
Binder jet printing
Soft magnetic materials
Iron-silicon-Boron alloy
Magnetic permeability
Intrinsic coercivity

ABSTRACT

Fe–Si alloys are an essential class of soft magnetic materials due to their high magnetic permeability and low hysteresis loss. Increasing the Si content above 3 wt% promotes coarser grain sizes and greater electrical resistivity, thereby enhancing the magnetic properties, such as magnetic permeability and specific loss density. However, the increased silicon content makes the machining challenging. Additive manufacturing technologies enable production of near net shape Fe–Si alloys with high silicon content, practically eliminating the machining challenges. This work investigated the effects of Si content, which ranged from 3 to 5 wt%, and B content, which ranged from 0 to 0.25 wt%, on the microstructure and magnetic properties. The Fe–Si–B alloys were binder jet printed, where the sintering temperature was varied between 1200 and 1250 °C, and microstructure-magnetic property relationships were investigated by characterizing the magnetic permeability, intrinsic coercivity, grain size, and density. The Fe-5wt.%Si alloy with 0.25% B sintered at 1200 °C exhibited the highest magnetic relative permeability (4447) and the lowest intrinsic coercivity (47.8 A/m).

* Corresponding author. Department of Chemical Engineering & Materials Science, Michigan State University, USA.
E-mail address: kumarige@msu.edu (G. Kumari).

https://doi.org/10.1016/j.matchemphys.2022.127181
Received 20 July 2022; Received in revised form 28 November 2022; Accepted 10 December 2022
Available online 12 December 2022

Table 1
The targeted compositions and sintering temperatures of the BJP samples processed using pure elemental powders.

Sample Number	Sample Composition	Boron Content (wt.%)	Sintering Temperature (°C)
1	Fe-3wt.%Si	0.00	1200
2	Fe-3wt.%Si	0.25	1200
3	Fe-5wt.%Si	0.00	1200
4	Fe-5wt.%Si	0.25	1200
5	Fe-3wt.%Si	0.00	1250
6	Fe-3wt.%Si	0.25	1250
7	Fe-5wt.%Si	0.00	1250
8	Fe-5wt.%Si	0.25	1250

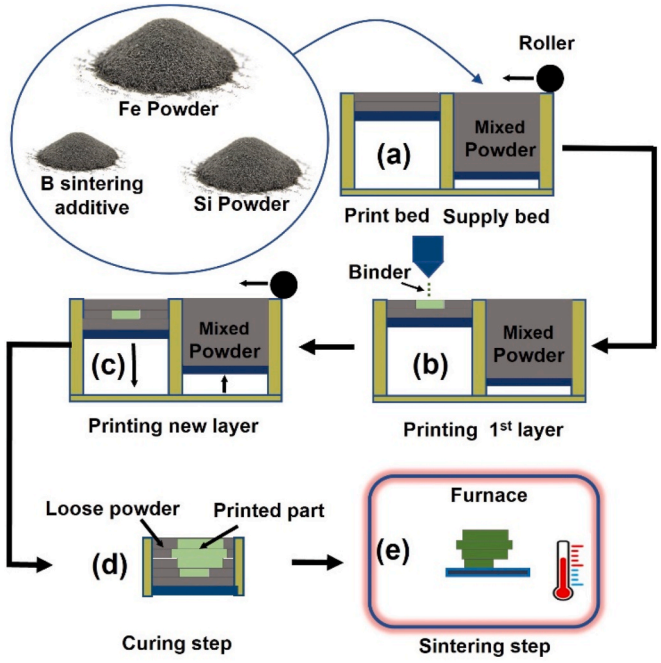

Fig. 1. A schematic depicting the binder jet printing (BJP) processing steps.

1. Introduction

Growing interest in electrification from energy-efficient and environmentally-friendly materials has increased the demand for high-performance soft magnetic materials (SMMs) [1]. SMMs, used in electrical machines, are subjected to time-varying magnetic fields [2–4]. The core loss, which impacts efficiency, is generally due to the magnetic properties of the SMMs. Increasing the silicon (Si) content to increase resistivity and decrease hysteresis loss can impact the efficiency of electrical machines. Low specific loss density at high excitation frequency can increase the machine's power density at high operating speeds. Improved electromagnetic performance, including torque, can be achieved with higher values of maximum relative permeability, indicative of improved magnetic flux flow within the soft magnetic material [3].

In the early 1900s, SMMs were popularly manufactured by melting iron (Fe) in a vacuum followed by alloying it with silicon (Si), which improved the permeability and magnetic properties of silicon steel [5,6]. Increasing the Si content is the most direct way to increase the electrical resistivity and magnetic permeability. However, Si contents greater than 4% lead to significant solid solution strengthening due to the formation of chemically-ordered phases like FeSi (ordered BCC, B_2) and Fe_3Si ($D0_3$ crystal structure) during slow cooling [2,3,7]. The presence of these hard and brittle phases results in poor workability, making such alloys less desirable for commercial applications. Over the past few decades, several studies have focused on synthesizing new Fe–Si SMMs by adding a third component, such as phosphorous (P), aluminum (Al), nickel (Ni), boron (B), lanthanum (La), to improve their properties [8–13]. Wan et al. added La and La + B as third element in SMC, which resulted in low core loss and high magnetic flux density compared to the SMC without any additions [13]. Also, the SMCs synthesized using Fe–Si–Ni powder exhibited stable permeability and high saturation flux density [12]. The addition of these third elements resulted in larger grain size and the formation of new phases, mainly on the grain boundaries, which contributed to low hysteresis and core loss [12,13].

Additive manufacturing (AM) creates physical 3D parts directly from computer-aided design (CAD) models as a result of the layer-by-layer consolidation of raw materials. AM processes significantly reduce the machining required to fabricate a part thereby enabling more efficient production of high Si (≥4% Si) SMMs with greater flexibility in producing desired geometries. Advancements in AM for processing magnetic materials have resulted in greater flexibility and efficiency to produce electrical machines [1,11–13]. AM processes provide flexibility in design not available with the conventional manufacturing processes. However, AM processing has not yet advanced in electrical field applications due to the lack of understanding of the microstructural evolution in printed parts. Various groups have worked on AM fabrication of electrical machine or electromagnets, but knowledge of microstructure-electrical and magnetic property relationships are still lacking [2,14]. More work is needed to improve the resulting microstructures processed using advanced AM techniques to achieve the desired magnetic properties.

Among the seven major American Standard Testing and Materials (ASTM) modes of 3D printing, fused deposition modeling, selective laser melting (SLM), and binder jet printing (BJP) dominate the AM processing of soft magnetic materials [15,16]. AM has resulted in limited formation of the ordered BCC phase in the SMMs because of the inter-layer cooling and sharp thermal gradient with SLM [17]. Metal powder-based AM processes, such as powder bed fusion utilize a heat source (high power laser or electron beam) to melt or fuse raw materials together for printing. In contrast, BJP is a solid-state AM technique, that utilizes a liquid bonding agent to join the powder in each layer selectively in a layer-by-layer fashion and subsequently sintering the printed part [18].

One of the major challenges for binder jet printing, where temperature below the melting temperature is used, is achieving samples with no porosity and shape distortion. Do et al. were able to achieve full density of BJP 316L stainless steel by adding B as a sintering aid [9]. Adding B reduced the sintering time and temperature, thereby enabling the densification of the final product more energy-efficiently without shape distortion. That was one of the reasons that B was used in the current work. In addition, the literature cited previously described the magnetic property enhancements achieved by the addition of B to Fe–Si alloys. Thus, these were the reasons motivating the B additions in the current work.

Pham et al. [19–21] demonstrated that BJP can be used to additively manufacture Fe–Si alloys with high permeability and low iron loss; however, discussion of the relationships between the magnetic properties and the microstructure was not provided. The current work investigated processing-microstructure-magnetic property relationships of the Fe–Si–B alloy system with varying Si and B contents, and a comparative study of the microstructure, magnetic relative permeability, and iron loss was performed using both pure elemental and pre-alloyed powders. The results indicate that both low hysteresis loss and high permeability are possible for B-modified Fe–Si alloys.

2. Materials and methods

In this study, eight different samples were BJP using pure elemental powders produced by American Elements followed by the

Table 2
The particle size and shape of the elemental powder used for BJP.

Powder		Average Particle Size (μm)	Shape
Main powder (Elemental)	Fe	90	Near spherical
	Fe	10	
	Si	1	
Sintering additive	B	1	N/A

N/A: Not available.

microstructural and magnetic property characterization. Two different Fe–Si ratios (Fe-3wt.%Si and Fe-5wt.%Si) were chosen and printed with and without 0.25 wt% B. The samples were printed then sintered at either 1200 °C or 1250 °C. The combination of the various conditions is summarized in Table 1.

2.1. Binder jet printing

BJP fabrication was performed using multi-step processing to obtain the desired shape of the printed parts. Firstly, a binder was injected on each powder layer. The injected binder phase penetrated through a given layer to connect with the previous layer. When all the layers were printed, the print bed was released to completely cure the printed part. After removing the loose powder, the final parts were densified through sintering. A schematic of the BJP process is provided in Fig. 1. Depending on the phases present in the process, sintering is classified as either solid-state sintering or liquid-phase sintering (LPS) [22–25]. In LPS, a small fraction of the material forms a liquid phase during the sintering process. The advantages of LPS over solid-state sintering include reduced sintering temperature, expediting the sintering process, to control the resulting microstructure, and reducing the residual porosity in the sintered products [24–26]. Selection of the binding agent and its volumetric quantity is important as low amounts of the binding agent can cause improper bonding, whereas excess binder can result in enlargements of printed lines [23]. Up to 20% linear shrinkage in sintered parts can occur due to the issues involving both the consolidation of the printed powder and shrinkage of the excessive binder. This can jeopardize the dimensional accuracy used in CAD models [14].

The BJP was performed using an ExOne X1-Lab machine. The feed powder-to-layer ratio was 2.3:1. Each printed layer was 150 μm in thickness with an initial spread velocity of 0.3 mm/s. The organic binder from ExOne's fluidfuse was used to print. The size and the shape of the powders used are summarized in Table 2. The Fe portion of the powder stock consisted of a mixture of 56 wt% of the larger average particle sizes (90 μm) and 44 wt% of smaller average particle sizes (10 μm), see Table 2. The Fe mixture was mixed with a certain amount of Si particles to control the Si content in the starting powder. A small amount of B as a sintering aid was also added to some of the powder mixtures.

After printing, the green samples were transferred into an air furnace and cured at 195 °C for 2 h to remove the binding agent. After curing, the samples were placed into a carbon-liner-resistance furnace (Material Research Furnaces, Allenstown, NH). The chamber was evacuated and purged with argon (Ar) at least three times to reduce the oxygen (O) content. Then, the chamber was filled to 906 psi with Ar and the temperature was raised to the sintering temperature (1200 °C and 1250 °C) at a ramp rate of 5 °C/min. After sintering for 6 h, the samples were furnace cooled at approximately 15 °C/min. The microstructural characterization was performed on the X–Y surface of the printed cube

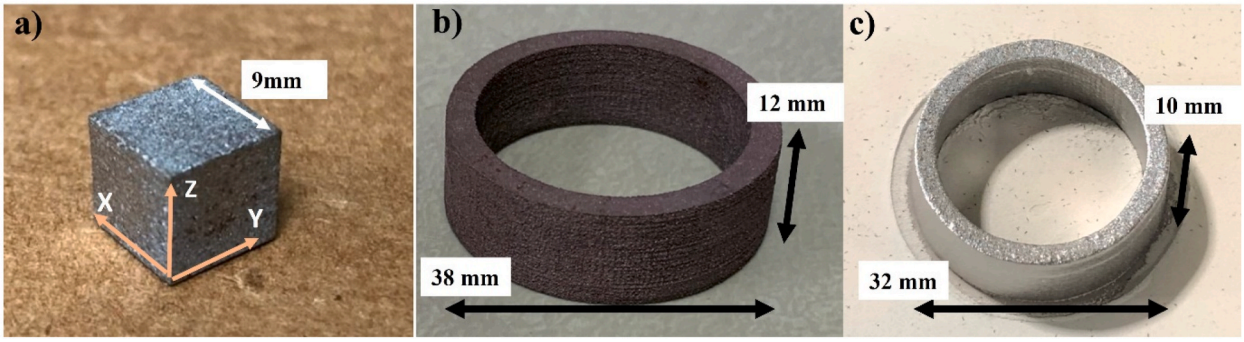

Fig. 2. Photographs of a) 3D-printed BJP sintered cube sample to show the printing direction nomenclature (Z is the printing direction), b) BJP ring (before sintering), c) BJP ring (after sintering).

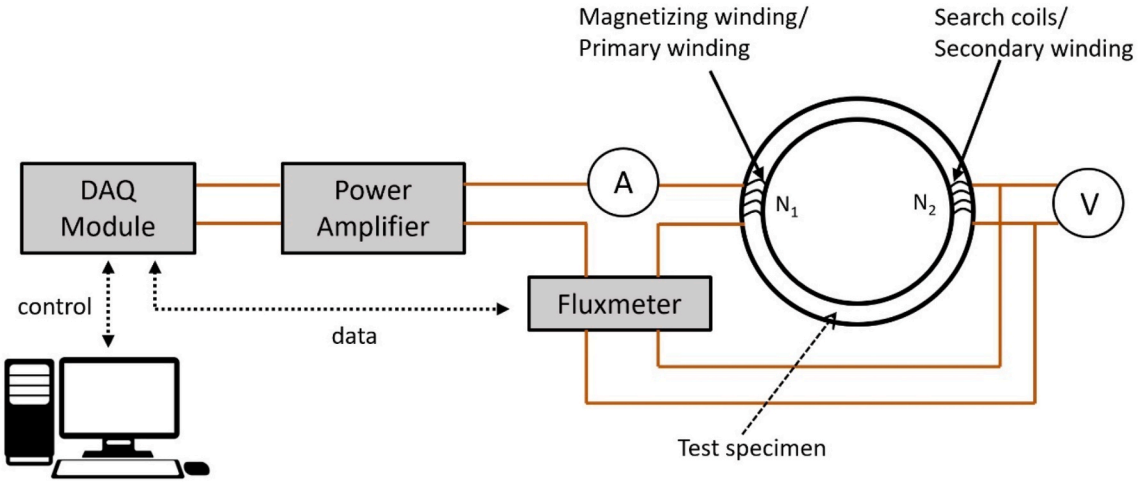

Fig. 3. Schematic of the experimental setup of the ring core DC/AC magnetic characterization.

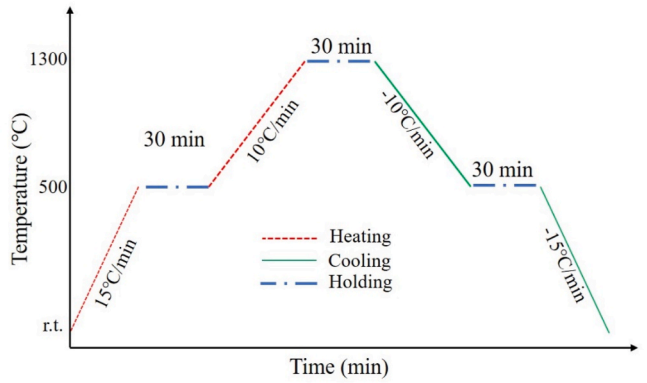

Fig. 4. Schematic of the heating cycle used for differential scanning calorimetry (DSC) characterization of samples no. 3 and 4.

sample where Z is the printing direction, Fig. 2a. Fig. 2b and c illustrate the printed rings before and after sintering, respectively. The magnetic property characterization was performed using the sintered ring shown in Fig. 2c.

2.2. Magnetic characterization

The magnetic characteristics are related to the microstructure of the material and were measured using the international standards in Refs. [27,28]. In particular, the specific iron loss density and the relationship between the magnetic field strength (H) and the magnetic induction (B) were characterized.

A commercially-available soft magnetic tester (Magnetic Instrumentation Model SMT-700) was used to evaluate the direct current (DC) and alternating current (AC) magnetic characteristics of BJP Fe–Si samples, see Fig. 3. Here, the power amplifier Model 7224 (Magnetic Instrumentation) was controlled via the data acquisition module to provide excitation to the primary winding. The measured excitation current, via the ammeter, was fed back to the computer to calculate the magnetic field strength H. The digital fluxmeter (Magnetic Instrumentation Model 2130) was used to measure the change in the magnetic flux induced in the secondary winding, which was related to the magnetic induction B. For each ring sample, there were 75 turns for the secondary windings and 100 turns for the primary windings, see Fig. 3.

For the DC characterization, quasi-static sinusoidal excitation at 1 Hz was used for the primary windings. The use of quasi-static excitation approximates the true DC characteristics of soft magnetic materials as the eddy current loss was negligible. The extracted magnetic properties for the DC characterization included the maximum relative permeability $\mu_{r,max}$, the intrinsic coercivity H_c, and the magnetic induction B at magnetic field strengths of 500 A/m and 10,000 A/m. Here, $\mu_{r,max}$ was the highest value of the relative permeability μ_r with respect to magnetic field strength H, as shown in equation below. The magnetic permeability in vacuum here was denoted as μ_0.

$$B = \mu_r \mu_0 H$$

For the AC characterization, the specific loss density of each BJP sample was extracted at excitation frequencies of 50, 200, and 400 Hz. Closed-loop control ensured that at each frequency the secondary-induced voltage remained sinusoidal, having a form factor within the range of $1.11 \pm 1\%$. The form factor was defined as the ratio between the average rectified value of the secondary voltage and the root-mean square value of the secondary voltage [28].

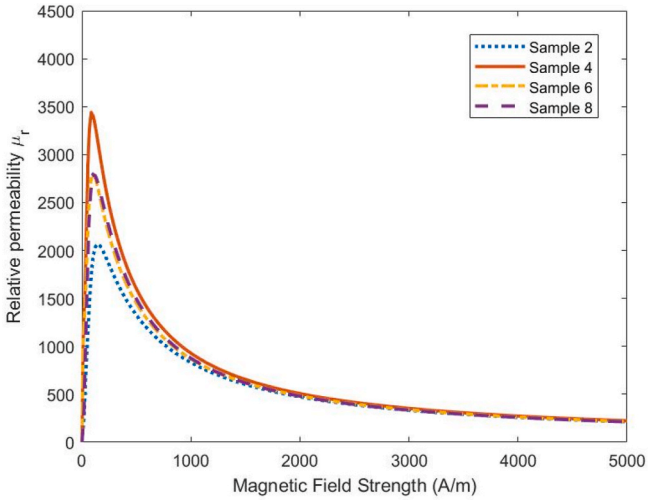

Fig. 5. Relative permeability curve $\mu_r - H$ of BJP Fe–Si ring samples containing B.

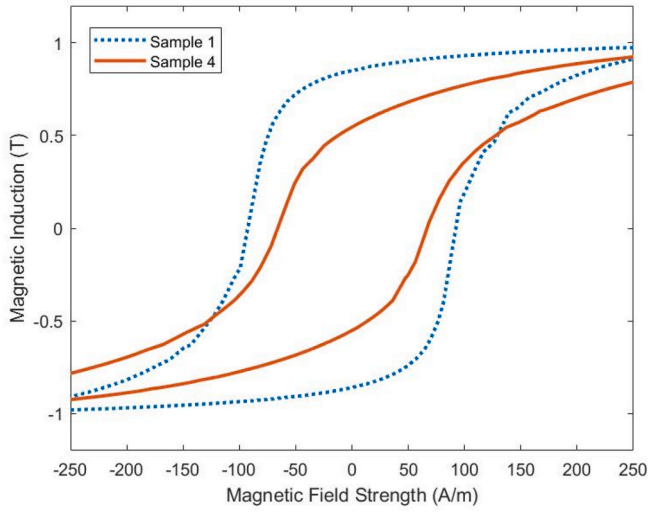

Fig. 6. Quasi-static hysteresis loop between the sample with the highest coercivity (Sample 1) and the sample with the lowest coercivity (Sample 4).

Table 3
A comparative table for magnetic properties including relative permeability, intrinsic coercivity, and magnetic induction for each sample.

Sample no.	1	2	3	4	5	6	7	8
Sample composition	Fe-3wt.%Si	Fe-3wt.%Si	Fe-5wt.%Si	Fe-5wt.%Si	Fe-3wt.%Si	Fe-3wt.%Si	Fe-5wt.%Si	Fe-5wt.%Si
Boron addition (wt%)	0	0.25	0	0.25	0	0.25	0	0.25
Sintering temperature (°C)	1200	1200	1200	1200	1250	1250	1250	1250
Relative permeability $\mu_{r,\ max}$ (H/m)	3461	2199	3262	3475	3134	2126	3179	2923
Intrinsic coercivity, Hc (A/m)	103.4	88.4	89.4	69.6	102.4	89.2	88.2	75.7
B@500 A/m (T)	1.08	0.85	1.03	1.01	1.09	0.83	1.03	0.95
B@10k A/m (T)	1.45	1.46	1.42	1.53	1.50	1.43	1.44	1.45
B@20k A/m (T)	1.60	1.61	1.54	1.75	1.66	1.60	1.59	1.61

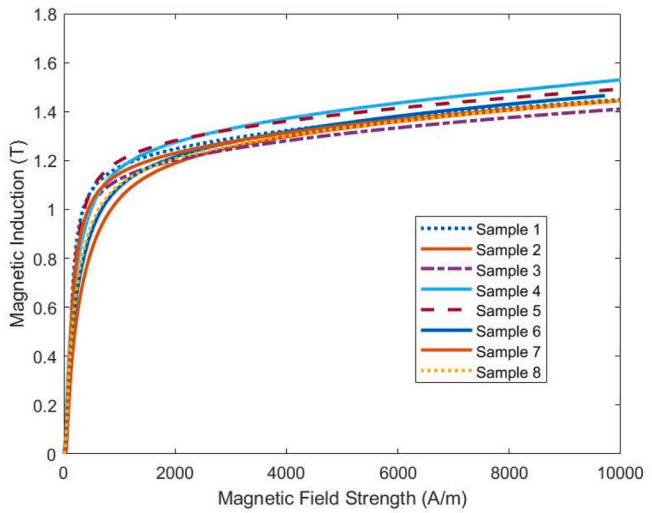

Fig. 7. Initial magnetization curves of the BJP Fe–Si samples. The magnetic induction at 10000A/m settled around 1.45T–1.55T.

2.3. Metallography

All sintered samples were metallographically prepared for microstructural evaluation. Samples were mechanically polished using through 400, 600, 800, 1200 US grit size (equivalent to FEPA 800, 1200, 2400, 4000 grit, respectively) SiC abrasive papers followed by diamond polishing with polycrystalline diamond paste of 6, 3, 1, 1/4 μm particle size using iso-propyl alcohol (IPA) as the lubricant. The final polishing was performed using colloidal silica solution (0.025 μm crystallite size, 50% diluted with IPA). To evaluate the grain boundaries and different phases, freshly prepared 5% Nital (5 mL nitric acid + 95 methanol) was used for swab etching for 30–60 s.

2.4. Materials characterization

Optical microscopy (OM), scanning electron microscopy (SEM), and x-ray diffraction (XRD) were used to characterize the microstructures. A Nikon eclipse MA200 optical microscope was used to take the images used for calculating the grain size via the line intercept method as per ASTM-E112-13 [29]. ImageJ software was used to help perform this calculation as well as the calculation of the volume fraction of the grain boundary phase present in the microstructures. XRD analysis was performed using a high-resolution Rigaku Ultima IV system equipped with a copper anode target (1.54 Å). XRD patterns were collected with an accelerating voltage of 40 kV, beam intensity of 44 mA in a Bragg Brentano configuration, and a 0.008step size within the range of $20^\circ < 2\theta < 120^\circ$. The spectra collected were analyzed using Rigaku software. Using a Tescan Mira3 field emission gun SEM, both secondary electron (SE) and backscattered electron (BSE) images were acquired. Energy dispersive spectroscopy (EDS) analysis was performed to investigate the composition of the phases inside the SEM using an acceleration voltage of 20 kV at a working distance of 12 mm. Electron backscattered

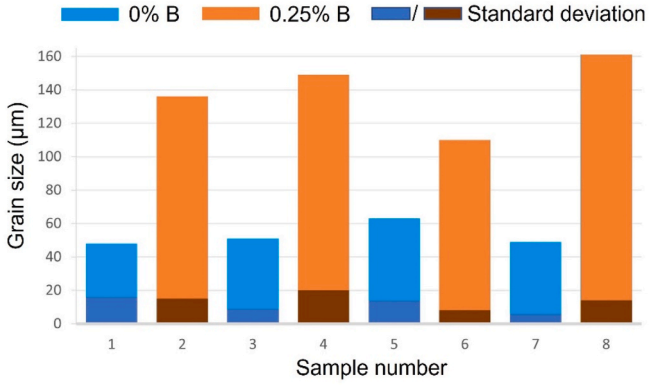

Fig. 9. Grain size comparison of all 8 samples.

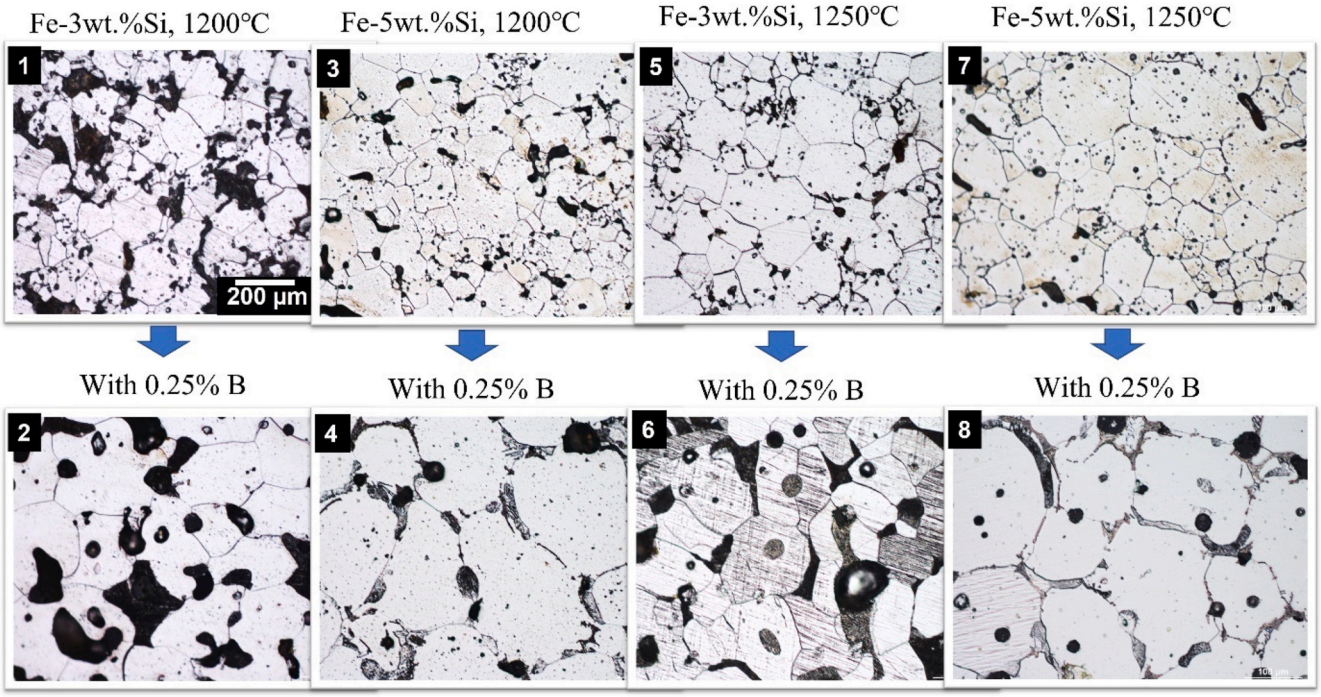

Fig. 8. Optical photomicrographs of the samples where the compositions and sintering compositions are indicated at the top and the sample number is indicated at the top-left corner.

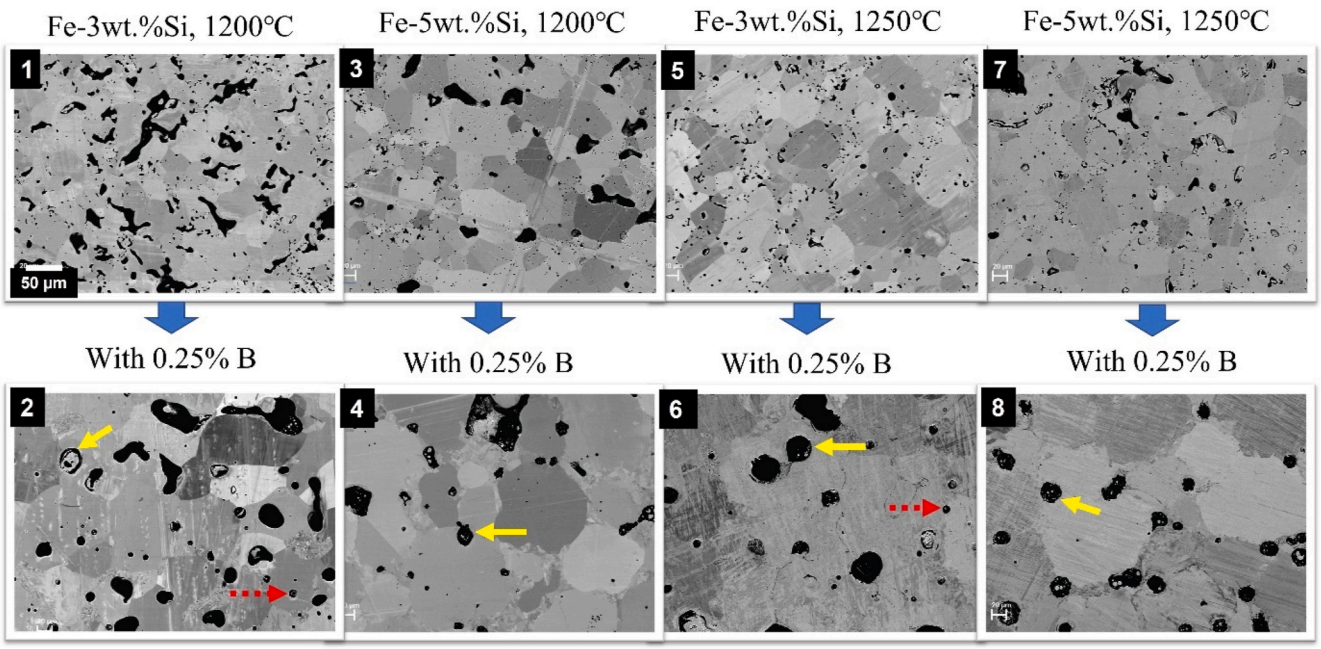

Fig. 10. BSE-SEM photomicrographs of the samples where the compositions and processing conditions are indicated on the top and the sample number is indicated at the top-left corner. The yellow solid arrow highlights oxides and the red dotted arrow highlights voids. (For interpretation of the references to colour in this figure legend, the reader is referred to the Web version of this article.)

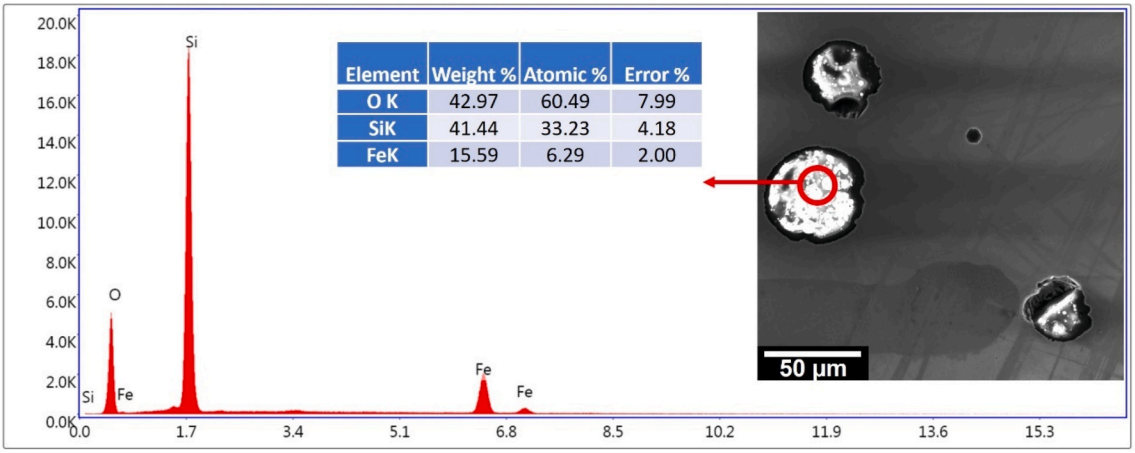

Fig. 11. SE−SEM photomicrograph of a region from sample 8 (Fe-5wt.%Si-0.25%B sintered at 1250 °C) containing precipitates. The EDS spectra of the region highlighted by the red circle is provided. (For interpretation of the references to colour in this figure legend, the reader is referred to the Web version of this article.)

diffraction (EBSD) orientation maps were collected using a Carl Zeiss Auriga SEM. These EBSD orientation maps were acquired at 20 keV beam voltage, working distances between 14 and 18 mm, and a step size of 2 µm with the specimen tilted 70° with respect to the electron beam. EBSD analysis software (EDAX TSL OIM analysis 6.1) was used to analyze the EBSD data considering 15° misorientations or higher as high-angle grain boundaries. Vickers microhardness measurements were performed using a Clark CM-800 AT hardness machine on different regions of the samples with a load of 0.2 kgf and dwell time of 15 s. The AM printed part's densities were calculated after sintering using the Archimedes' principle in IPA. Differential scanning calorimetry (DSC), using a Netzsch DSC model STA 449 F3 Nevio, was conducted on sample 3 (Fe-5wt.%Si; sintered at 1200 °C) and sample 4 (Fe-5wt.%Si-0.25 wt% B; sintered at 1200 °C) weighing 77.4 mg and 119.8 mg, respectively, to identify the phase transformations as a function of the temperature. A platinum (Pt) crucible with an Al_2O_3 liner was used for the heat-treatments. The reaction chamber was purged with a continuous flowing (70 mL/min) Ar gas. The temperature range and the heating rate used for data collection were 500–1300 °C and 10K/min respectively, see Fig. 4.

3. Results and discussion

3.1. Magnetic properties

The specific loss density and maximum relative permeability, acquired from AC and DC characterization, respectively, were compared. Under DC characterization, the relative permeability was the highest with a value of ~3500 for sample 4 (i.e., Fe-5wt.%Si- 0.25%B sintered at 1200 °C). The addition of B increased the maximum relative permeability with Fe_5Si_5 sintered at 1200 °C. However, lower Si content and higher temperature resulted in lower relative permeability when B was added, see Table 3. As shown in the.

μ_r-H curve of Fig. 5, the Fe-5wt.%Si-0.25 wt%B sintered at 1200 °C

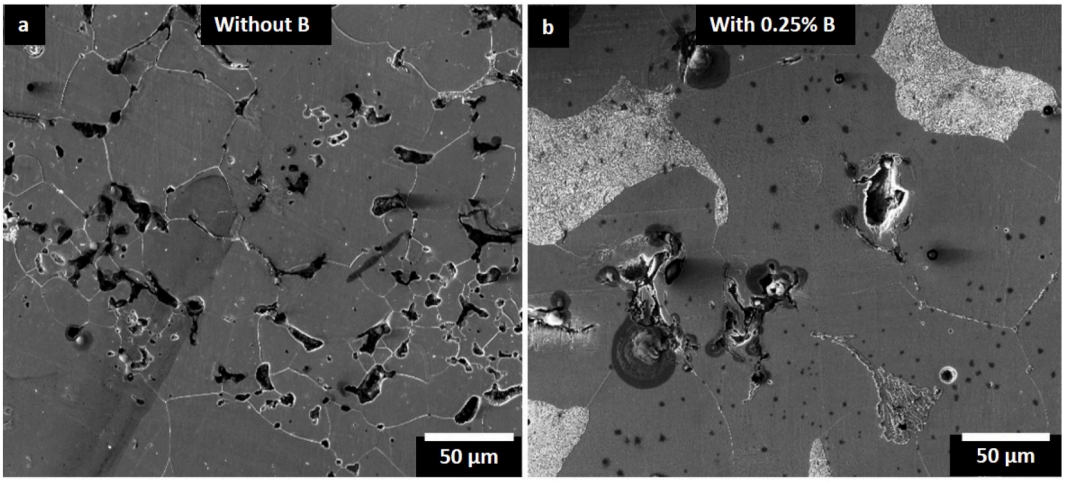

Fig. 12. SE−SEM photomicrographs of (a) Fe-3wt.%Si sintered at 1200 °C (Sample 1), (b) Fe-3wt.%Si-0.25%B sintered at 1200 °C (Sample 2).

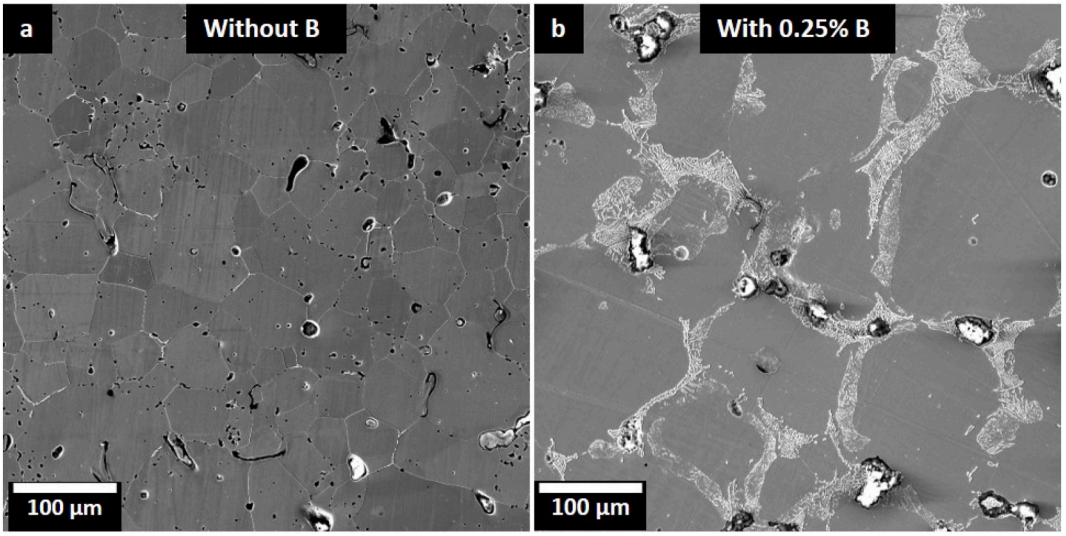

Fig. 13. SE−SEM photomicrographs of (a) Fe-5wt.%Si sintered at 1200 °C (Sample 3), (b) Fe-5wt.%Si-0.25%B sintered at 1200 °C (Sample 4).

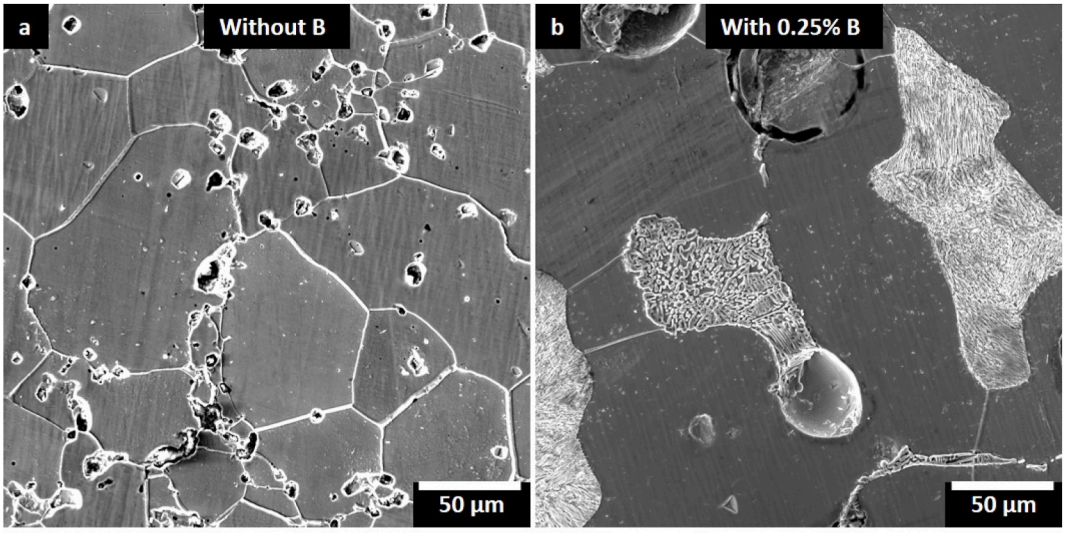

Fig. 14. SE−SEM photomicrographs of (a) Fe-3wt.%Si sintered at 1250 °C (Sample 5), (b) Fe-3wt.%Si −0.25%B sintered at 1250 °C (Sample 6).

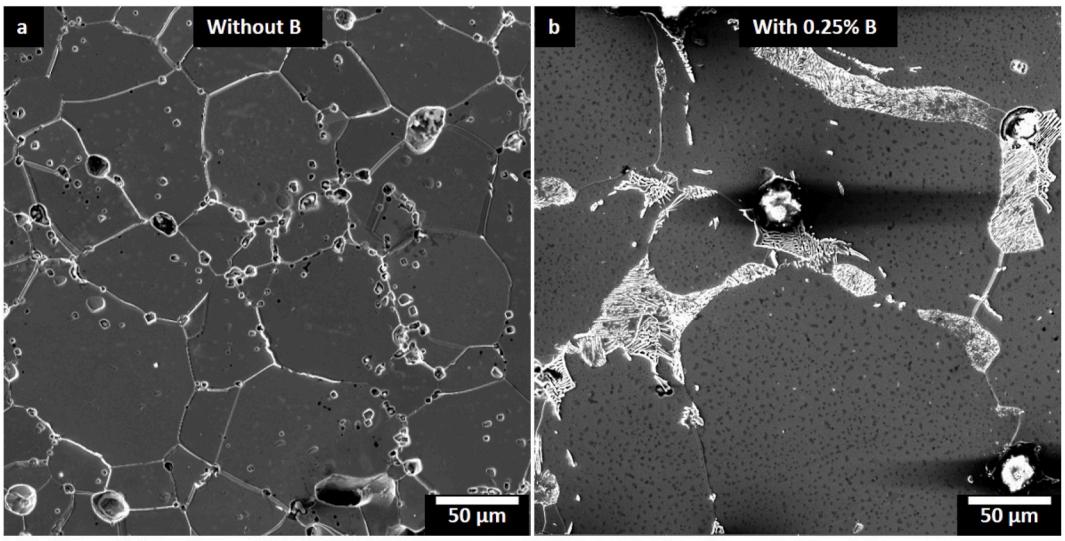

Fig. 15. SE–SEM photomicrographs of (a) Fe-5wt.%Si sintered at 1250 °C (Sample 7), (b) Fe-5wt.%Si- 0.25%B sintered at 1250 °C (Sample 8).

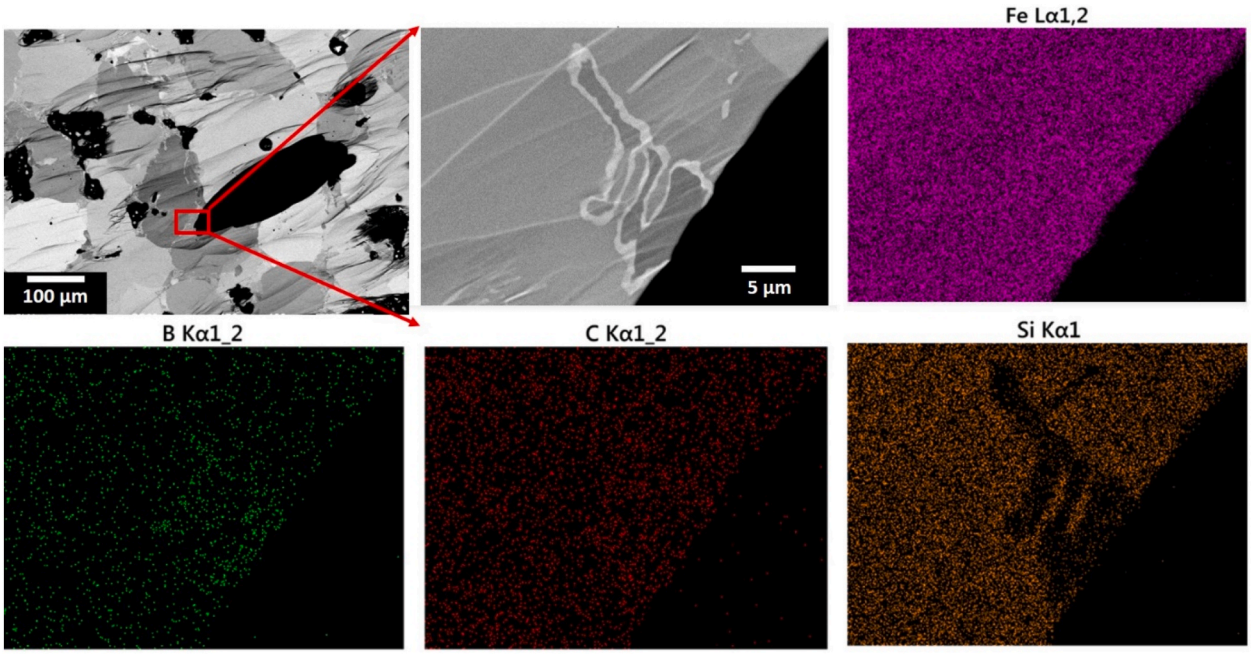

Fig. 16. SEM EDS elemental mapping results for sample 4 (Fe-5wt.%Si-;0.25% B sintered at 1200 °C).

(sample 4) exhibited the highest relative permeability. When Fe-3wt.% Si-0.25 wt%B was sintered at 1250 °C (sample 8), its maximum relative permeability was ~60% that of sample 4.

A lower coercivity value indicates a lower hysteresis loss in the sample, which benefits the performance of the electrical machine, especially at low operating speeds [30]. The intrinsic coercivity was found to be lowest with a value of 69.6 A/m for sample 4 (Fe-3wt.%Si-0.25% B sintered at 1200 °C), whereas it was found to be the highest for sample 1 (Fe-3wt.%Si sintered at 1200 °C) with a value of 103.4 A/m, as illustrated in the B–H curve on Fig. 6. The B additions in the samples helped reduce the intrinsic coercivity value, which was beneficial for reducing the hysteresis loss of the material. This reduction in loss due to B addition was observed when the samples were sintered at both 1200 °C and 1250 °C. However, the increase of 50 °C in sintering temperature did not show any improvement in the magnetic properties.

The higher magnetic induction at each magnetic field strength indicates that an electrical machine can require less excitation to reach a specific electromagnetic performance [6]. This is beneficial to the machine. The magnetic induction at 10000A/m, as shown in Fig. 7, indicated that all of the samples settled around 1.45T–1.55T, which is typically seen in commercial soft magnetic materials, such as soft magnetic composites.

3.2. Microstructure

3.2.1. Optical microscopy

The effects of the Si and B content and the sintering temperature on the microstructures were initially studied using optical microscopy, see Fig. 8, which compares allF 8 samples. Coarse grains are favorable for permeability and magnetic induction, since a single grain can accommodate multiple magnetic domains with a lesser domain wall energy (anisotropy energy) [31–33]. The addition of 0.25% B resulted in an

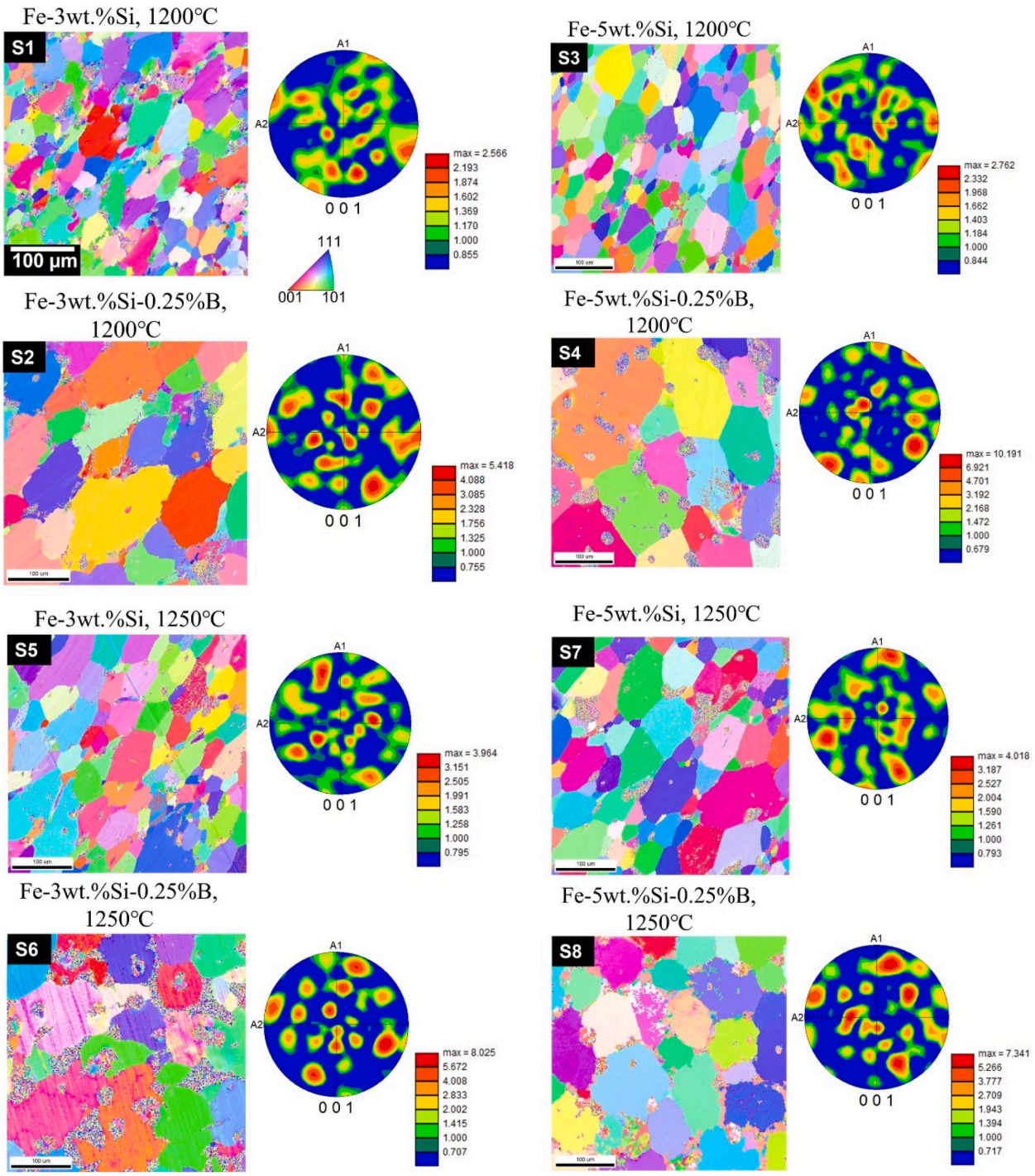

Fig. 17. Representative EBSD inverse pole figure (IPF) and associated 001 pole figure (PF) for each sample, where the sample compositions and sintering temperature are indicated on the top of each IPF and the sample number is indicated at top-left corner.

increased grain size, see Fig. 9. Sample 8 (Fe-5wt.%Si 0.25%B at 1250 °C) exhibited the largest grain size (160 μm) due to the combination of the B addition and the highest sintering temperature of 1250 °C. Sample 4, having similar compositions as sample 8 (Fe-5wt.%Si 0.25%B sintered at 1250 °C), but sintered at a lower temperature (1200 °C), exhibited a grain size of 148 μm. Grain boundary acts as a barrier that interferes with the domain movement during magnetization. Hence, coarse grain size benefits low hysteresis loss and core loss. Following Fig. 9, all the samples with B exhibited the larger grain sizes compared to the corresponding samples without B, and hence, a lower loss was measured in all the samples with B, see Table 3.

The samples with B tended to exhibit rounded corners at the grain boundaries, while the samples without B tended to exhibit irregularly shaped grain boundaries or sharp corners at the grain boundaries, as exhibited on Fig. 8. The sharp corners are good for the low coercivity as they act as nucleation sites for domains, whereas the grain boundaries act as a pinning sites/barriers to the magnetic domain propagation [6]. The samples without B exhibited grain boundaries with sharper corners and therefore acted as nucleation sites for domains, but grain boundary pinning was dominant here due to the smaller grain sizes in comparison to the samples containing B. Hence, the samples without B exhibited higher intrinsic coercivity and loss density compared to the samples with

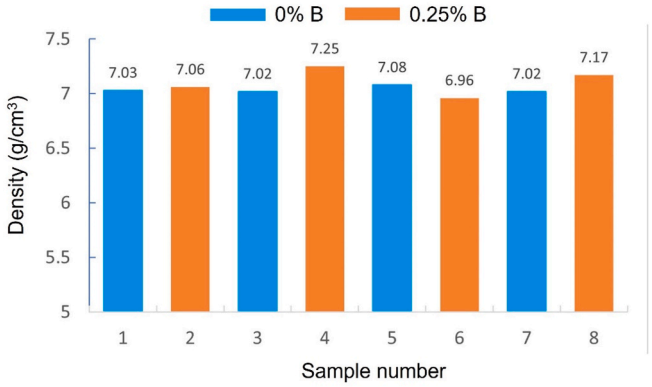

Fig. 18. Absolute density comparison of all the samples.

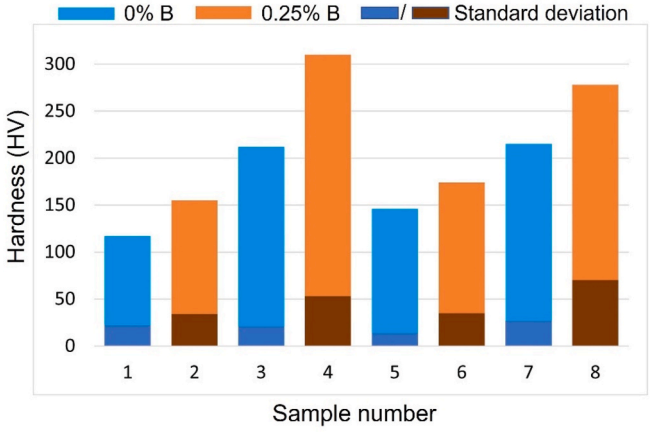

Fig. 19. Vickers hardness for all eight samples.

B.

3.2.2. Scanning electron microscopy

Fig. 10 shows representative BSE-SEM images of all eight samples. Samples without B resulted in a channel of pores or interconnected pores along grain boundaries that could have retarded the grain growth and created irregularly shaped and smaller grains compared to the samples containing B. The addition of B reduced the pore content and also resulted in spherical or closed pores. Irrespective of the B addition, both increasing the Si content from 3 wt% to 5 wt% and increasing the sintering temperature from 1200 °C to 1250 °C resulted in decreased porosity. The B-containing samples also exhibited particles (black chunky structure) in addition to small voids, which are highlighted in Fig. 10 with yellow solid arrows for the black chunky particles and red dotted arrows for the voids. EDS characterization of the particles suggested that they were oxides rich in Fe and Si. Fig. 11 shows one such oxide particle from sample 8 (Fe-5wt.%Si-0.25%B)

sintered at 1250 °C).

Fig. 12 compares the Fe-3wt.%Si samples sintered at 1200 °C, where sample 1 (Fig. 12a) has no B and sample 2 (Fig. 12b) has 0.25%B. Fig. 13 compares the Fe-5wt.%Si samples sintered at 1200 °C, where sample 3 (Fig. 13a) has no B and sample 4 (Fig. 13b) has 0.25%B. Fe-3wt.%Si (sample 5) and Fe-3wt.%Si with 0.25% B (sample 6) sintered at 1250 °C were compared in Fig. 14 to elucidate the effect of B addition. Fig. 15 shows a comparison of the Fe-5wt.%Si samples sintered at 1250 °C, where sample 7 (Fig. 15a) has no B and sample 8 (Fig. 15b) has 0.25%B. Figs. 12–15 show that adding 0.25% B resulted in a grain-boundary lamellae phase that emanated from the liquid phase formed during sintering process. According to the Fe–B phase diagram, the addition of B results in a eutectic reaction of Fe_2B and Fe at 1174 °C, which shows as grain-boundary lamellae phase [34]. For the samples having identical compositions ($Fe_{95}Si_5$ with 0.25%B), the lamellae phase area percentage was around 7% when sintered at 1200 °C, whereas it was only 4% when sintered at 1250 °C. To estimate the phase composition, EDS analysis was performed. Fig. 16 indicates that the lamellar Fe_2B phase from sample 4 was B rich and Si poor. EDS mapping detected the presence of a relatively small amount of carbon (C). To quantify the C content, a glow discharge spectrometry was conducted using LECO GDS900. It showed the existence of C with an average value of 0.12 wt%. Most likely this C content was the unburned residue from the organic binder used during the printing. The secondary phase act as nucleation sites for magnetic domains if they are ferromagnetic in nature [6].The grain boundary Fe_2B phase decreased the coercivity by acting as nucleating sites and hence, improved the soft magnetic properties by decreasing both the hysteresis loss and specific loss density compared to the samples without B.

Texture plays an important role in determining the permeability of soft magnets. For soft magnet Fe–Si steel, the preferred crystallographic direction is < 001> type due to the lowest magneto-crystalline anisotropy, which is the easy magnetization direction [6]. To assess the texture of the samples, EBSD orientation maps were collected. Fig. 17 shows the inverse pole figures (IPF) and 001 pole figures (PF) for each of the eight different microstructures. The texture intensity was highest for the sample 4 (Fe-5wt.%Si-0.25%B sintered at 1200 °C) with a value of 10.2 times random texture. Since the BJP process does not melt the particle during printing, grain growth occurred during the sintering only, however the grains did not grow in a preferred orientation. The samples containing B exhibited higher texture intensity, ranging from 5.4 to 10.2 times random texture for the (001) pole figure, which may explain the greater permeability exhibited by these samples compared to those without B.

3.3. Other characterizations (density, hardness, XRD)

A comparison of the absolute density of each sample is provided in Fig. 18. The addition of B resulted in an increase in the density in every case. Fe-5wt.%Si-0.25%B sintered at 1200 °C (sample 4) exhibited the highest density ~ 7.25 g/cm^3, which was consistent with the magnetic properties trend shown in Table 3. The sample with the same composition as sample 4, but sintered at 1250 °C, exhibited a slightly lower density ~7.17 g/cm^3. Generally, the densification increases with increase in sintering temperature, but in the case of sample 4 (Fe-5wt.%Si-0.25%B) sintering at 1200 °C caused a liquid phase formation at 1174 °C which resulted the highest density than sample 8.

An increase in Si content to Fe alloy leads to B_2 (α_2) phase ordering and α_1 ($D0_3$) phase ordering in existence with the disordered BCC iron (A_2) [5,7]. Following the Fe–Si binary equilibrium phase diagram, the ordered phases (α_1, α_2) are present for temperatures between 1200 and 1220 °C and dissolve at around 1250 °C [7,35,36]. Thus, sintering at 1250 °C could result in a decrease in hardness due to dissolution of the ordered phases. Notable effect of Si and B contents, and sintering temperature were observed in the Vickers hardness data shown on Fig. 19. With the increase in Si content from 3 to 5%, the hardness value significantly increased. For example, the hardness difference between sample 1 (Fe-3wt.%Si) and sample 3 (Fe-5wt.%Si) was 95 VHN. Increasing both the Si and B contents also resulted in increased hardness values. For example, sample 1 (Fe-3wt.%Si) exhibited a hardness of 117 VHN, whereas sample 4 (Fe-5wt.%Si-0.25%B) exhibited a hardness value of 310 VHN. For the Fe-5wt.%Si samples with the addition of 0.25%B, a change in sintering temperature from 1200 °C (sample 4) to 1250 °C (sample 8) resulted in a decrease in the hardness from 310 to 275 HV, respectively. Sample 4 (Fe-5wt.%Si-0.25%B sintered at 1200 °C) exhibited the greatest hardness value and this could be a result of the presence of the ordered α_2 phase.

XRD results indicated the diffraction peaks of α phase (BCC) iron as

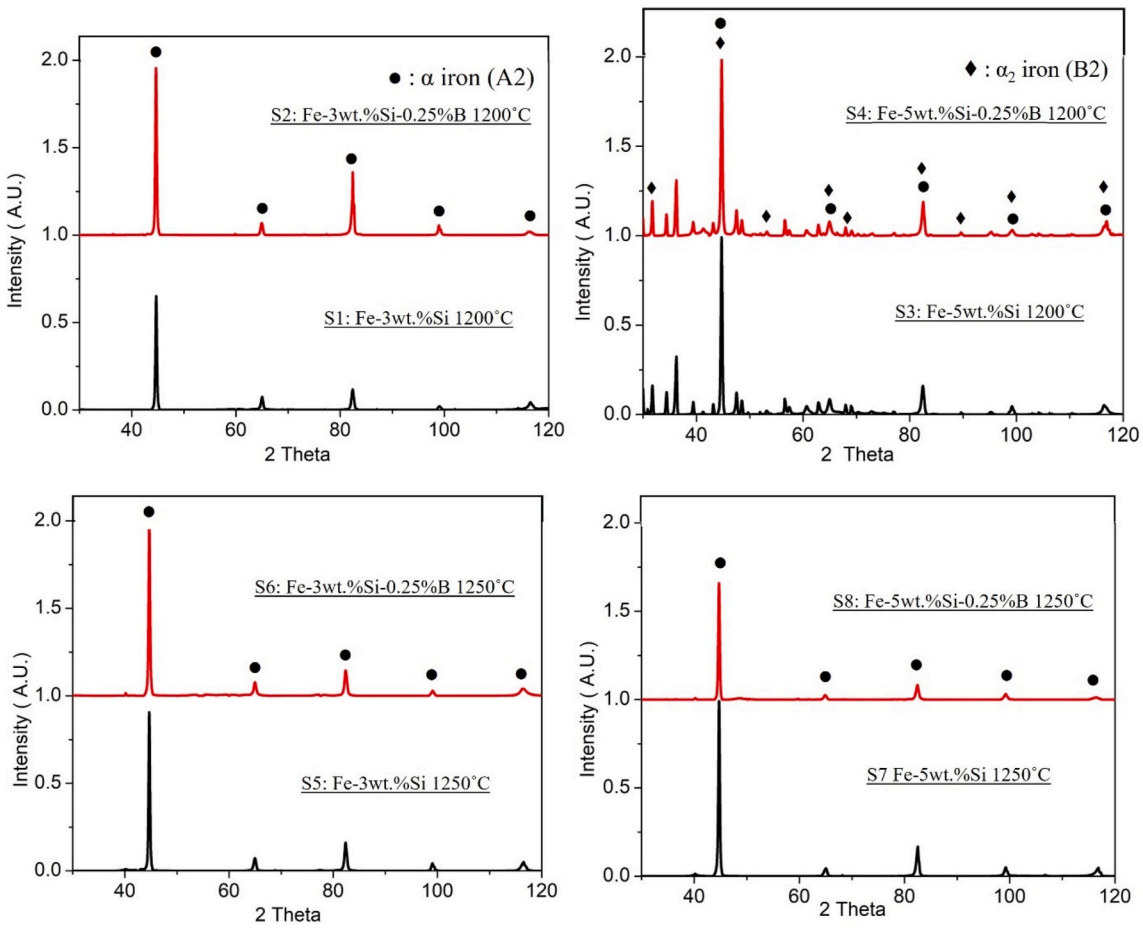

Fig. 20. X-Ray diffraction intensity versus 2-theta plots for all the samples.

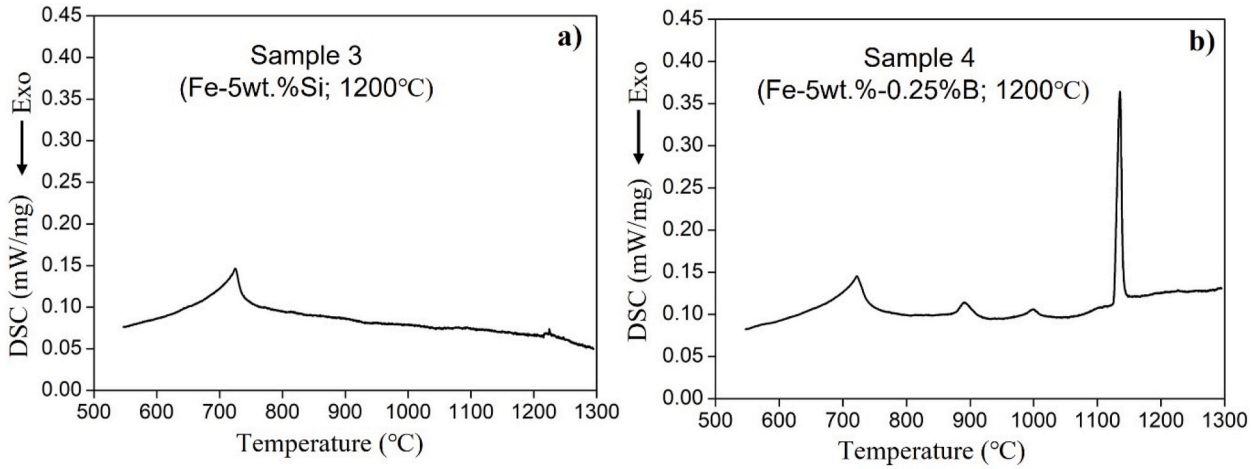

Fig. 21. Differential scanning calorimetry (DSC) of sample 3 (Fe-5wt.%Si sintered at 1200 °C) and sample 4 (Fe-5wt.%Si-0.25%B sintered at 1200 °C) heating rate of 10 K/min from 500 to 1300 °C.

shown in Fig. 20. There was little difference in the relative heights of the peaks between the samples having 0.25% B and no B. The grain boundary Fe_2B lamellae phase (tetragonal) peaks were not visible, possibly due to a small fraction. Sample 3 (Fe-5wt.%Si sintered at 1200 °C) and sample 4 (Fe-5wt.%Si-0.25%B sintered at 1200 °C) exhibited several peaks that were not exhibited by the other samples as shown in Fig. 20. We could not index some of the peaks that were uniquely present in sample 3 and 4, and this will be the focus of the future work. The superlattice peaks from the ordered BCC (α_2) phase were indexed and found to be overlapping with some of the BCC (α) disordered phase peaks. If we compare the magnetic properties of the samples shown in Table 3, it appears that the samples containing ordered phases has improved the magnetic properties. The combined effect of 0.25% B addition, which exhibited in both a larger grain size and a grain boundary lamellae phase, and sintering at 1200 °C, which resulted in ordered phases, enhanced the magnetic properties, especially

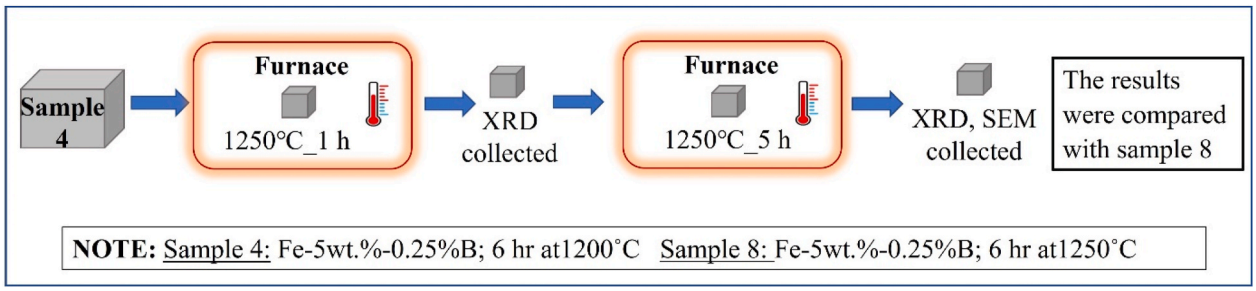

Fig. 22. Heat-treatment of sample 4 (Fe-5wt.%Si-0.25%B sintered at 1200 °C) for phase dissolution exploration.

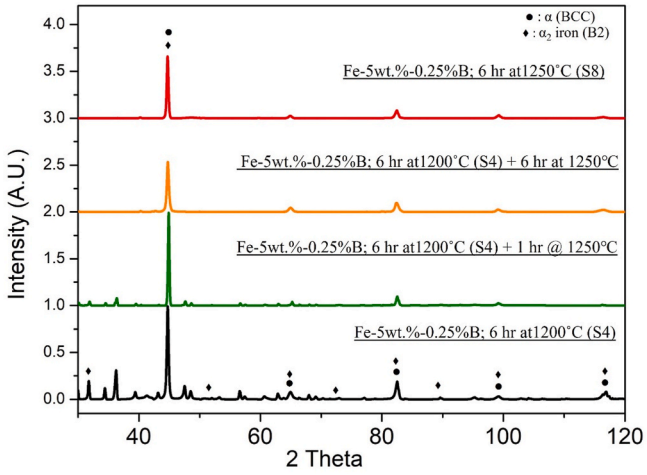

Fig. 23. XRD intensity versus 2-theta plots of sample 4 (bottom), sample 4 heat-treated at 1250 °C for 1hr, sample 4 heat-treated at 1250 °C for 6hr, and sample 8 (top).

for the samples having composition $Fe_{95}Si_5$. Hence, the sample 4 (Fe-5wt.%Si-0.25%B sintered at 1200 °C) exhibited the best magnetic properties among all the samples.

3.4. Detailed study of sample 4 (Fe-5wt.%Si-0.25%B sintered at 1200 °C)

The above discussion makes clear that the sample with 5% Si and 0.25%B, sintered at 1200 °C (sample 4) resulted in the best magnetic properties (lower coercivity and higher permeability) among all combination of parameters. As seen in the XRD pattern in Fig. 20, the samples having 5% Si and sintered at 1200 °C exhibited extra peaks from ordered phases. A further study was conducted to understand the reasoning behind the exhibition of the better magnetic properties of sample 4. It was important to confirm the difference between the two samples with 5% Si sintered at 1200 °C with B (sample 4) and without B (sample 3). A DSC study was conducted on these two samples. The heating curve from 500 to 1300 °C is provided in Fig. 21. Fig. 21a shows DSC results for sample 3 (Fe-5wt.%Si sintered at 1200 °C), while Fig. 21b shows the curve for sample 4 (Fe-5wt.%Si-0.25%B sintered at 1200 °C). The curves indicated the endothermic peaks at 725 °C (for sample 3) and 722 °C (for sample 4) with an integrated area of 21.4 J/g and 20.7 J/g, respectively. The curie transformation temperature for Fe–Si alloys can vary in the range of 770-720 °C depending on the Si

Table 4
The particle size and shape of the pre-alloyed powders mixture used for BJP.

Powder		Average Particle Size (μm)	Shape
Pre-alloyed powder	Fe_8Si	45 ± 15	Near spherical
Elemental powder	Fe	10	
Sintering additive	B	1	N/A

N/A: Not available.

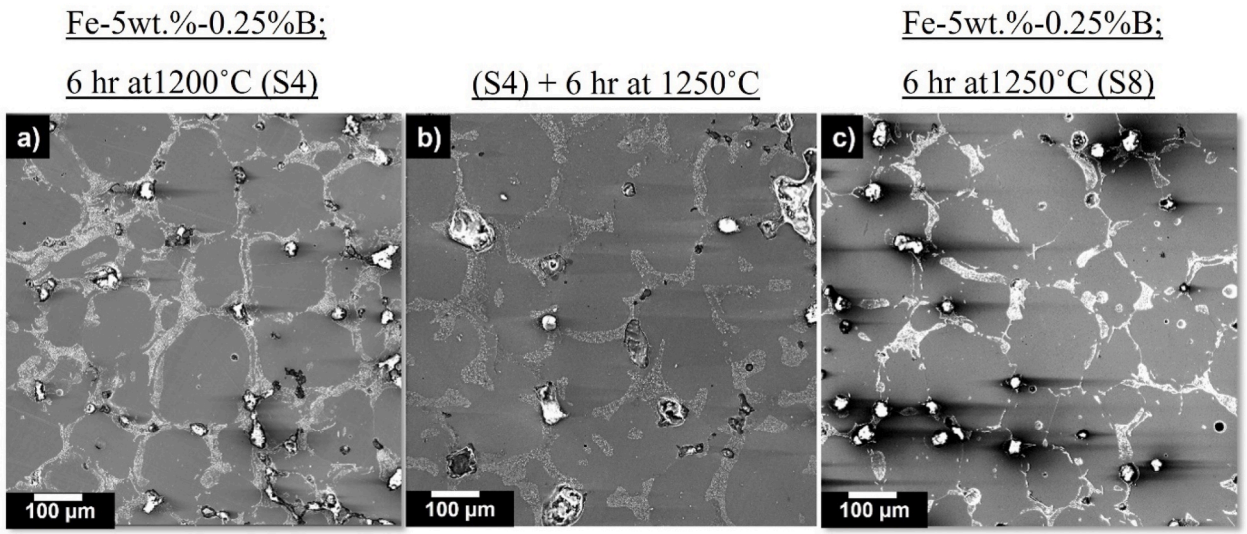

Fig. 24. A SE−SEM micrographs of a) sample 4 (Fe-5wt.%Si-0.25%B sintered at 1200 °C) b) Sample 4+heat-treated @1250 °C for 6 h, c) Sample 8 (Fe-5wt.%Si-0.25%B sintered at 1250 °C).

Table 5
Magnetic properties and density comparison for sample 4 and sample 8 having Fe-5wt.%Si-0.25%B sintered at 1200 °C using a) elemental powder (sample 4), b) pre-alloyed powder (sample 9).

Sample number	4	9
Powder type	AE	PA + AE
Sample composition sintered at 1200°C for 6 h in Ar environment	Fe-5wt.%Si-0.25 wt%B	Fe-5wt.%Si-0.25 wt%B
Density (g/cc)	7.24	7.44
Hardness (HV)	310 ± 42	332 ± 30
Relative permeability, $\mu_{r,\ max}$	3475	4447
Intrinsic coercivity Hc (A/m)	69.6	47.77
B@500A/m (T)	1.00	1.09
B@10 kA/m (T)	1.53	1.53
B@20 kA/m (T)	1.75	1.75

AE: American elements, PA: pre-alloyed.

content [35,37]. Hence, the above peaks correspond to the curie transformation. Sample 4 (Fig. 21b) shows three other endothermic peaks at 891, 1000, and 1135 °C with an integrated area of 2.91, 1.74, and 12.92 J/g, respectively. Referring to the Fe–B binary phase diagram, the peak at 1135 °C correlates to the Fe_2B phase. The presence of the Fe_2B lamellae phase was consistent with the SEM and EDS results. Other peaks at 891 °C and 1000 °C did not show any corresponding weight loss in the thermo-gravimetric analysis (TGA) curve, therefore they were considered to be related to the allotropic transformation of the Fe phases.

A comparative study was conducted on sample 4 (Fe-5wt.%Si-0.25% B sintered at 1200 °C) and sample 8 (Fe-5wt.%Si-0.25%B sintered at 1250 °C) to understand the effects of the difference in sintering temperature. In Fig. 20, we can see that the XRD pattern of sample 4 (bottom) exhibited extra peaks compared to sample 8 (top). Therefore, to understand the role of the sintering temperature, an additional heat-treatment was conducted on sample 4 as shown in Fig. 22. Sample 4 was systematically heat-treated at 1250 °C for 6 h. XRD patterns from the heat-treated samples (after 1 h and 6 h heat-treatment) were collected and compared to the patterns of sample 4 and sample 8 as shown in Fig. 23. Heating sample 4 at 1250 °C for 6 h resulted in the dissolution of the extra phases initially present in sample 4 (see bottom in Fig. 23). The XRD results of the heat-treated sample looked similar to those for sample 8 (see top in Fig. 23). SE−SEM photomicrographs were also collected to observe any change occurring due to heating at a higher temperature (1250 °C). In Fig. 24, sample 4 (Fig. 24a) exhibits a continuous grain boundary phase, whereas the heat-treated sample (Fig. 24b) and sample 8 (Fig. 24c) showed a discontinuity in the grain boundary phase. The discontinuity came from the dissolution of Fe_2B lamellae phases when heated to 1250 °C. From the magnetic data in Table 3, it is evident that sample 4, which contained the continuous grain boundary phase, provided better soft magnetic properties. We also compared the magnetic properties of samples without B. Sample 7 (Fe-5wt.%Si sintered at 1250 °C) resulted in lower intrinsic coercivity and higher magnetic induction than sample 3 (Fe-5wt.%Si sintered at 1200 °C). Hence, sintering at 1250 °C provided better magnetic

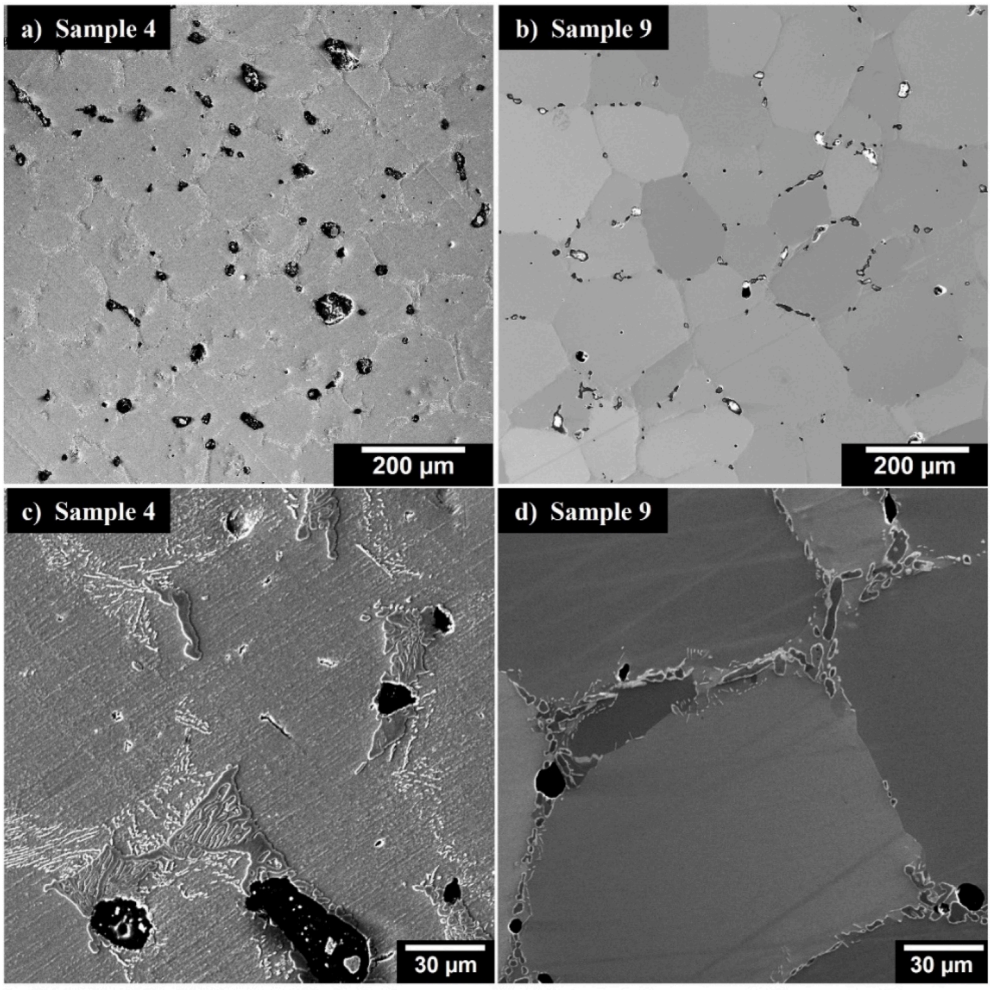

Fig. 25. SEM photomicrographs of samples having Fe-5wt.%Si 0.25%B sintered at 1200 °C using (a+c) elemental powder (sample 4) and (b + d) pre-alloyed powder (sample 9), (a), (b), (c) were taken in SE mode while (d) was taken in BSE mode.

properties than sintering at 1200 °C for the samples without B. But the addition of B enables samples to be sintered at 1200 °C while still exhibiting attractive magnetic properties. A detailed study involving crystal structure identification and composition analysis is planned to find the microstructural difference between sample 4 (Fe-5wt.%Si 0.25%B sintered at 1200 °C) and other samples.

3.5. Pre-alloyed powder sample

Among the various 3D printing methods, the BJP technique consolidates the printed powders primarily based on diffusion. All the samples used so far were printed using pure elemental powder, i.e., pure Fe and Si powder. It is difficult to estimate the equilibrium solidus and liquidus temperatures using pure powders as the BJP process relies on very large diffusion distances for phase formation and to obtain complete homogenization. To obtain more homogenous conditions in shorter times, a mixture of pre-alloyed powder with elemental powder was used, see Table 4 for powder detail. Based on the above eight samples' results, sample 4 (Fe-5wt.%Si-0.25%B sintered at 1200 °C) was selected as due to its resulting microstructure such as large grain size and highest density and magnetic properties such as highest permeability and lowest intrinsic coercivity. Hence, to attain the similar chemistry and sintering temperature, sample 9 (Fe-5wt.%Si-0.25%B sintered at 1200 °C) was printed using the powder mixture. The mixture contained ~66.8 wt% of pre-alloyed powder, ~32.9 wt% of pure Fe, and 0.25 wt% of B powder, specified in Table 4. Magnetic and microstructural characterizations were conducted, and the results were compared. As shown in Table 5, the relative permeability of sample 9 was nearly 28% higher than sample 4 while the intrinsic coercivity reduced more than 30%. The improvements in permeability and coercivity were achieved with negligible impact to the saturation flux density. The saturation flux density was maintained with the pre-alloyed powder, see Table 5.

The SEM photomicrographs in Fig. 25 (a and b) indicate that there was a significant difference in the microstructure between two samples. The average grain size of the pre-alloyed sample was calculated to be 156 μm, which was slightly larger than that for the elemental powder sample, which exhibited an average grain size of 148 μm. Compared to the elemental powder (sample 4), the pre-alloyed powder (sample 9) produced less oxide and finer voids at the grain boundary. A higher density and hardness, 7.44g/cc and 332 HV, respectively, see Table 5, was observed for sample 9. The smaller voids and larger grain size supported the higher permeability and low coercivity. In the study of Cramer et al. [14], it is noted that a Fe-6.5 wt%Si alloy exhibited a hardness value of 3.9 GPa, which was greater than that for either sample 4 (3.04 GPa) or sample 9 (3.26 GPa) of the current study, and this is expected due to the higher amount of Si present. Assessing the micrographs at a higher magnification, the Fe_2B lamellae were found to be continuous on the grain boundaries in the pre-alloyed powder sample, whereas they were discontinuous along the boundaries in the elemental powder sample, refer Fig. 25 (c & d). Since the lamellae phase is acting as a nucleation site for the magnetic domains, continuity along the grain boundaries helped in improving the magnetic permeability for sample 9.

4. Summary and conclusions

In this work, Fe–Si soft magnetic materials produced by BJP were studied. The effect of 1) increase in Si content, 2) sintering temperature change, and 3) B addition as a sintering additive on magnetic properties were studied.

- The microstructure, intrinsic coercivity, and permeability of binder jet processed steels ranging in Si between 3-5 wt% and B between 0 and 0.25 wt% were investigated using the microstructural correlation.
- The addition of B resulted in larger grain sizes, less porosity, increased density due to the formation of the Fe_2B lamellae ferromagnetic phase at the grain boundaries.
- In case of B added samples, the intrinsic coercivity decreased and relative permeability improved with increasing Si content from 3 to 5 wt%. But for the samples without B, increasing the Si content from 3 to 5 wt% resulted in decreased coercivity without any improvement in permeability. The trend of relative permeability change is not consistent and the reasoning should be studied in the future work.
- Fe-5wt.%Si with 0.25%B sintered at 1200 °C exhibited larger grain size, high density and ordered phases, which resulted in the most attractive combination of intrinsic coercivity (69.6 A/m) and permeability (3475 H/m) among all the samples.
- Compared with the elemental powder, the pre-alloyed powder resulted in larger grain sizes and less porosity and improved magnetic properties. The greater microstructural homogeneity may have been the reason for this.

CRediT authorship contribution statement

Geeta Kumari: Methodology, Investigation, Writing – original draft, Data curation, except for the magnetic data part. **Thang Q. Pham:** Conceptualization, Methodology, Investigation, Writing – original draft, the original draft for the magnetic part. **Hawke Suen:** Conceptualization, Methodology, Investigation, Writing – review & editing. **Tanzilur Rahman:** Investigation, Writing – review & editing. **Patrick Kwon:** Conceptualization, Writing – review & editing, Supervision, Project administration, Funding acquisition. **Shanelle N. Foster:** Conceptualization, Writing – review & editing, Supervision, Project administration, Funding acquisition. **Carl J. Boehlert:** Writing – review & editing, Supervision, Project administration.

Declaration of competing interest

The authors declare that they have no known competing financial interests or personal relationships that could have appeared to influence the work reported in this paper.

Data availability

Data will be made available on request.

Acknowledgment

The authors would like to thank the Department of Navy, Office of Naval Research for sponsoring this work, under ONR Award Number N00014-18-1-2514. The authors also would like to acknowledge Dr. Per Askeland from Michigan State University and Dr. Nicholas J. Jones from Naval Surface Warfare Centre for the experimental support.

References

[1] B. Yang, Z. Wu, Z. Zou, R. Yu, High-performance Fe/SiO2 soft magnetic composites for low-loss and high-power applications, J. Phys. D Appl. Phys. 43 (36) (2010), https://doi.org/10.1088/0022-3727/43/36/365003.
[2] T.N. Lamichhane, L. Sethuraman, A. Dalagan, H. Wang, J. Keller, M. P. Paranthaman, Additive manufacturing of soft magnets for electrical machines—a review, Mater. Today Phys. 15 (2020), 100255, https://doi.org/10.1016/j.mtphys.2020.100255.
[3] J.M. Silveyra, E. Ferrara, D.L. Huber, T.C. Monson, Soft magnetic materials for a sustainable and electrified world, Science 362 (6413) (2018), https://doi.org/10.1126/science.aao0195, 80.
[4] H. Shokrollahi, K. Janghorban, Soft magnetic composite materials (SMCs), J. Mater. Process. Technol. 189 (1–3) (2007) 1–12, https://doi.org/10.1016/j.jmatprotec.2007.02.034.
[5] F. González, Y. Houbaert, A review of ordering phenomena in iron-silicon alloys, Rev. Metal. (Madr.) 49 (3) (2013) 178–199, https://doi.org/10.3989/revmetalm.1223.

[6] B.D. cullity, C.D. graham, Introduction to Magnetic Materials, second ed., Wiley & son, 2009.
[7] Y.I. Ustinovshchikov, I.V. Sapegina, Ordering of Fe-Si phases, Inorg. Mater. 41 (1) (2005) 24–31, https://doi.org/10.1007/s10789-005-0006-3.
[8] D. Sharma, K. Chandra, P.S. Misra, Design and development of powder processed Fe-P based alloys, Mater. Des. 32 (6) (2011) 3198–3204, https://doi.org/10.1016/j.matdes.2011.02.046.
[9] T.M. Do, T.J. Bauder, H. Suen, K. Rego, J. Yeom, P. Kwon, Additively manufactured full-density stainless steel 316L with binder jet printing, in: ASME 13th International Manufacturing Science and Engineering Conference MSEC2018, 2018, pp. 1–10, https://doi.org/10.1115/MSEC2018-6681.
[10] S. Mirzababaei, S. Pasebani, A review on binder jet additive manufacturing of 316L stainless steel, J. Manuf. Mater. Process. 3 (3) (2019) 8–12, https://doi.org/10.3390/jmmp3030082.
[11] X. Peng, et al., Design and fabrication of Fe–Si–Al soft magnetic composites by controlling orientation of particles in a magnetic field: anisotropy of structures, electrical and magnetic properties, J. Mater. Sci. 54 (11) (2019) 8719–8726, https://doi.org/10.1007/s10853-019-03470-3.
[12] W. Xu, C. Wu, M. Yan, Preparation of Fe-Si-Ni soft magnetic composites with excellent high-frequency properties, J. Magn. Magn Mater. 381 (2015) 116–119, https://doi.org/10.1016/j.jmmm.2014.12.073.
[13] Y. Wan, W.Q. Chen, S.J. Wu, Effects of lanthanum and boron on the microstructure and magnetic properties of non-oriented electrical steels, High Temp. Mater. Process. 33 (2) (2014) 115–121, https://doi.org/10.1515/htmp-2013-0039.
[14] C.L. Cramer, et al., Binder jet additive manufacturing method to fabricate near net shape crack-free highly dense Fe-6.5 wt.% Si soft magnets, Heliyon 5 (11) (2019), e02804, https://doi.org/10.1016/j.heliyon.2019.e02804.
[15] W.E. Frazier, Metal additive manufacturing: a review, J. Mater. Eng. Perform. 23 (6) (2014) 1917–1928, https://doi.org/10.1007/s11665-014-0958-z.
[16] A. Paolini, S. Kollmannsberger, E. Rank, Additive manufacturing in construction: a review on processes, applications, and digital planning methods, Addit. Manuf. 30 (September) (2019), 100894, https://doi.org/10.1016/j.addma.2019.100894.
[17] T.D. Susan, et al., Additive Manufacturing of Soft Ferromagnetic Alloys (LENS and Powder Bed), 2018.
[18] E. Sachs, M. Cima, P. Williams, D. Brancazio, J. Cornie, Three dimensional printing: rapid tooling and prototypes directly from a CAD model, J. Manuf. Sci. Eng. Trans. ASME 114 (4) (1992) 481–488, https://doi.org/10.1115/1.2900701.
[19] T.Q. Pham, S. Member, H. Suen, P. Kwon, S.N. Foster, S. Member, Reduction in hysteresis loss of binder jet printed iron silicon, Int. Conf. Electr. Mach. (2020) 1669–1675, https://doi.org/10.1109/ICEM49940.2020.9270774.
[20] T.Q. Pham, et al., Binder jet printed iron silicon with low hysteresis loss, in: 2019 IEEE Int. Electr. Mach. Drives Conf. IEMDC 2019, 2019, pp. 1045–1052, https://doi.org/10.1109/IEMDC.2019.8785256.
[21] T. Pham, H. Suen, P. Kwon, G. Kumari, C. Boehlert, S. Foster, Reduction in hysteresis loss of binder jet printed iron silicon with boron, IEEE Trans. Ind. Appl. 57 (5) (2021) 4864–4873, https://doi.org/10.1109/TIA.2021.3099463.
[22] V.A. Ivensen, Densification of Metal Powders during Sintering, 1973.
[23] A. Mostafaei, et al., Binder jet 3D printing—process parameters, materials, properties, modeling, and challenges, Prog. Mater. Sci. 119 (June 2020) (2021), 100707, https://doi.org/10.1016/j.pmatsci.2020.100707.
[24] P.E. Zovas, R.M. German, K.S. Hwang, C.J. Li, Activated and liquid-phase sintering—progress and problems, JOM J. Miner. Met. Mater. Soc. 35 (1) (1983) 28–33, https://doi.org/10.1007/BF03338181.
[25] R.M. German, Supersolidus liquid-phase sintering of prealloyed powders, Metall. Mater. Trans. A Phys. Metall. Mater. Sci. 28 (7) (1997) 1553–1567, https://doi.org/10.1007/s11661-997-0217-0.
[26] J. Liu, A. Lal, R.M. German, Densification and shape retention in supersolidus liquid phase sintering, Acta Mater. 47 (18) (1999) 4615–4626, https://doi.org/10.1016/S1359-6454(99)00320-1.
[27] V. Method, E. Frame, Standard test method for alternating-current magnetic properties of materials at low inductions using the wattmeter-varmeter-ammeter-, in: ASTM International, 1998, pp. 1–5, 03, no. April 1993.
[28] ASTM International, Standard Test Method for Direct Current Magnetic Properties of Materials Using D-C Permeameters and the Ballistic Test Methods 1, 2000, pp. 7–12.
[29] A. International, Standard Test Methods for Determining Average Grain Size, 2010, pp. 1–27, https://doi.org/10.1520/E0112-13.1.4. *Astm E112-13*.
[30] G.E. Fish, Soft magnetic materials, in: Proc. IEEE, vol. 78, 1990, pp. 947–972, https://doi.org/10.1109/5.56909, 6.
[31] M. Shiozaki, Y. Kurosaki, The effects of grain size on the magnetic properties of nonoriented electrical steel sheets, J. Mater. Eng. 11 (1) (1989) 37–43, https://doi.org/10.1007/BF02833752.
[32] X.F. Bi, Y. Tanaka, K. Sato, K.I. Arai, K. Ishiyama, Y. Yamashiro, The relationship of microstructure and mangentic properties in colled-rolled 6.5% Si-Fe alloy, IEEE Trans. Magn. 32 (5) (1996) 4818–4820.
[33] G.Y. Chin, J.H. Wernick, Soft magnetic metallic materials, Handb. Ferromagn. Mater. 2 (C) (1980) 55–188.
[34] A. Szewczyk-nykiel, The effect of the addition of boron on the densification , microstructure and properties of sintered 17-4 Ph stainless steel, Tech. Trasactions, Mech. 2–M (2014) 86–96.
[35] O. Kubaschewski, Iron Binary Phase Diagram 53 (9) (1982).
[36] J.H. Yu, et al., The effect of heat treatments and Si contents on B2 ordering reaction in high-silicon steels, Mater. Sci. Eng. A 307 (2001) 29–34.
[37] V. Chaudhary, S.A. Mantri, R.V. Ramanujan, R. Banerjee, Additive manufacturing of magnetic materials, Prog. Mater. Sci. 114 (February 2019) (2020), 100688, https://doi.org/10.1016/j.pmatsci.2020.100688.